

Activated lone-pair electrons lead to low lattice thermal conductivity: a case study of boron arsenide

Guangzhao Qin,^{1, 2, a)} Zhenzhen Qin,³ Huimin Wang,^{4, 2} and Ming Hu^{2, b)}

¹⁾*Institute of Mineral Engineering, Division of Materials Science and Engineering, Faculty of Georesources and Materials Engineering, RWTH Aachen University, Aachen 52064, Germany*

²⁾*Department of Mechanical Engineering, University of South Carolina, Columbia, SC 29208, USA*

³⁾*International Laboratory for Quantum Functional Materials of Henan, and School of Physics and Engineering, Zhengzhou University, Zhengzhou 450001, China*

⁴⁾*College of Engineering and Applied Science, Nanjing University, Nanjing 210023, China*

(Dated: 26 May 2022)

Reducing thermal conductivity (κ) is an efficient way to boost the thermoelectric performance to achieve direct solid-state conversion to electrical power from thermal energy, which has lots of valuable applications in reusing waste resources. In this paper, we propose an effective approach for realizing low κ by introducing lone-pair electrons or making the lone-pair electrons stereochemically active through bond nanodesigning. As a case study, by cutting at the (111) cross section of the three-dimensional (3D) cubic boron arsenide (*c*-BAs), the κ is lowered by more than one order of magnitude in the resultant two-dimensional (2D) system of graphene-like BAs (*g*-BAs) due to the stereochemically activated lone-pair electrons. However, this does not naturally happen to all materials. For instance, breaking the perfect octahedral coordination of 3D diamond as in the 2D graphene adversely enhances thermal transport. The underlying mechanism is analyzed based on the comparative study on the thermal transport properties of *g*-BAs, *c*-BAs, graphene, and diamond (*c*-BAs \rightarrow *g*-BAs *vs.* diamond \rightarrow graphene). Furthermore, deep insight into the electronic origin is gained by performing fundamental analysis on the electronic structures. Similar concept can be also extended to other systems with lone-pair electrons beyond BAs, such as group III-V compounds (*e.g.* BN, AlN, GaN, *etc.*), where a strong correlation between κ modulation and electronegativity difference for binary compounds is found. Thus, the lone-pair electrons combined with a small electronegativity difference could be the indicator of lowering κ through bond nanodesigning to change the coordination environment. The proposed approach for realizing low κ and the underlying mechanism uncovered in this study would largely benefit the design of thermoelectric devices with improved performance, especially in future research involving novel materials for energy applications.

I. INTRODUCTION

Due to the ability of firsthand solid-state conversion to electrical power from thermal energy, especially for waste heat reusing, thermoelectrics have attracted a lot of attention in recent years¹. Thermoelectrics have lots of valued applications in recovering resources and thus may make crucial contributions to the crisis of environment by solving energy problems². Moreover, thermoelectrics possess the advantages of having no moving components and being environmentally friendly compared to traditional mechanical heat engines. Generally, the thermoelectric efficiency and performance can be characterized by a dimensionless figure of merit³

$$ZT = S^2 \sigma T / \kappa, \quad (1)$$

where S , σ , T and κ are thermopower (Seebeck coefficient), electrical conductivity, absolute temperature and

total thermal conductivity, respectively. The commercial applications in industry of thermoelectric devices are currently limited by the low ZT merit. To approach the Carnot coefficient as closely as possible, a high energy generation efficiency is necessary, which corresponds to a large ZT merit. Based on the definition [Eq. (1)], lowering the κ would be more efficient to boost the ZT merit due to the inversely proportional relation⁴.

Previous theoretical studies predicted that cubic boron arsenide (*c*-BAs) in the bulk form has an exceptionally high κ over 2000 W/mK, which is comparable to the bulk carbon crystals (diamond) with record highest κ ⁵. The ultra-high κ of *c*-BAs was analyzed to be resulted from the large phonon band gap between acoustic and optical phonon branches together with the bunching of the acoustic phonon branches, which reduce phonon-phonon scattering⁵. The features of the phonon dispersion of *c*-BAs analyzed based on first-principles calculations are then confirmed by experimental measurements based on inelastic *x*-ray scattering⁶. By considering the phonon-phonon scattering involving four phonons, Feng *et al.*⁷ found that the κ of *c*-BAs reduces from 2200 to 1400 W/mK, which was recently confirmed by experi-

^{a)}Electronic mail: qin.phys@gmail.com

^{b)}Electronic mail: hu@sc.edu

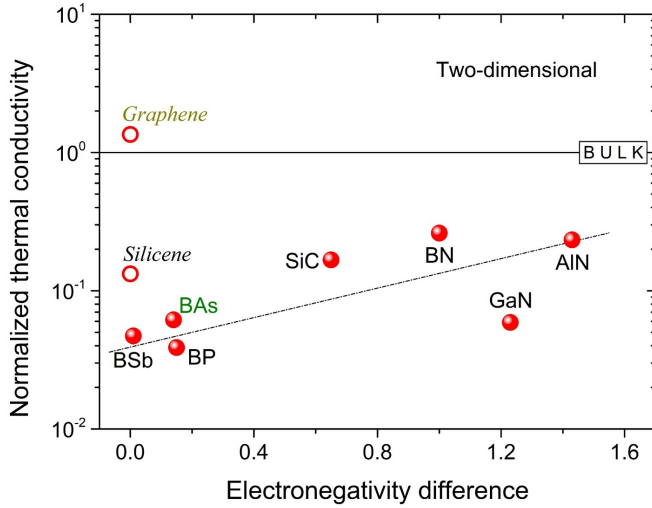


FIG. 1. The κ of typical two-dimensional materials (graphene, silicene, BN, AlN, GaN, BP, BAs, BSb, and SiC) at 300 K, which are normalized to the bulk counterparts, respectively. The two-dimensional materials possess lower κ compared to the bulk counterparts, except graphene. The dot line is for an eye guide. The specific data can be found in Supplemental Table 1.

mental studies^{8–10}. Experimental measurements reveal that the κ of BAs can be suppressed by the arsenic deficiency or vacancy in the BAs sample¹¹ and the phonon-boundary scattering in BAs microstructures^{12,13}. However, the obtained κ of BAs is still too high that limits its potential applications in thermoelectrics, despite that the Seebeck coefficient and thermoelectric power factor of BAs is comparable to those of bismuth telluride,¹³ which is one of the most commonly used thermoelectric materials. Thus, it would be meaningful if one can find an effective approach to lower the intrinsic κ of BAs to benefit its applications in thermoelectrics. Moreover, the approach that makes such a high κ material applicable for thermoelectrics would also largely benefit the design of thermoelectric devices with improved performance by lowering κ , especially in the future research involving novel materials for energy applications.

In this paper, we propose an effective approach for realizing low κ by bond nanodesigning to make the lone-pair electrons stereochemically active. As a result, much lower κ can be generally achieved, except the case of graphene (Fig. 1). As a specific case study, when transforming the three-dimensional (3D) *c*-BAs into the two-dimensional (2D) graphene-like BAs (*g*-BAs), the κ is found to be lowered by more than one order of magnitude (Fig. 2) due to the stereochemically activated lone-pair electrons. The underlying mechanism is analyzed based on the comparative study on the thermal transport properties of *g*-BAs, *c*-BAs, graphene, and diamond, considering the similarity of the transformation from 3D cubic to 2D honeycomb planar geometry structures (*c*-BAs \rightarrow *g*-BAs *vs.* diamond \rightarrow graphene) but the opposite trend for the κ modula-

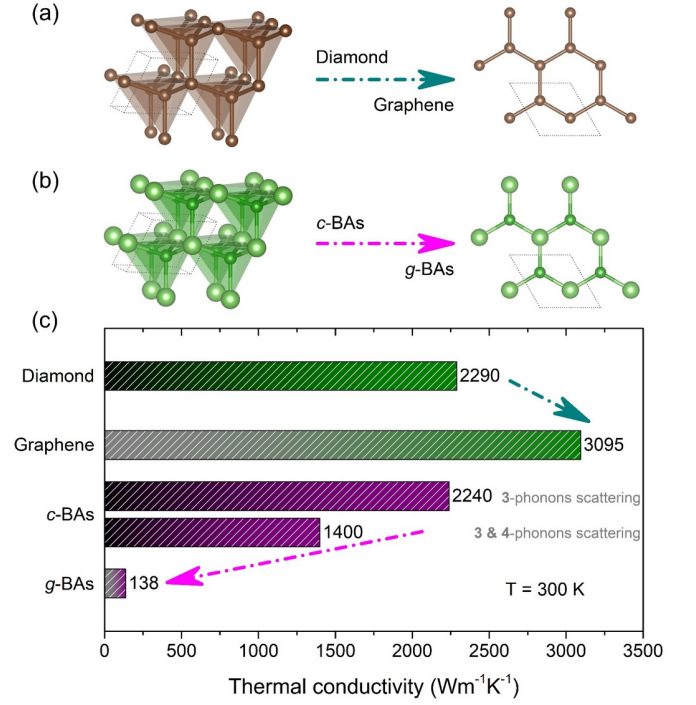


FIG. 2. The similarity of the transformation from 3D cubic to 2D honeycomb planar geometry structures (*c*-BAs \rightarrow *g*-BAs *vs.* diamond \rightarrow graphene) is in contrast to the opposite κ variation. When transforming from 3D into 2D, the κ of BAs is found to be anomalously lowered by more than one order of magnitude. (a) The structure of graphene in 2D is the (111) cross section of the structure of diamond in 3D, which is planar due to the sp^2 hybridization of carbon atoms. (b) The *g*-BAs to *c*-BAs is like graphene to diamond. (c) The comparison of κ of diamond, graphene, *c*-BAs,^{5,7} and *g*-BAs.

tion. Moreover, deep insight into the electronic origin is gained by performing fundamental analysis on the electronic structures.

II. RESULTS AND DISCUSSIONS

A. The anomalously low κ of *g*-BAs

By cutting the 3D cubic structure of *c*-BAs at the (111) cross section, *g*-BAs can be obtained with similar planar honeycomb structure as graphene (*c*-BAs \rightarrow *g*-BAs *vs.* diamond \rightarrow graphene). The κ of *g*-BAs is obtained to be 137.70 W/mK, which is more than one order of magnitude lower than that of graphene (3094.98 W/mK). Note that only 3-phonons scattering is considered here for simplicity. The κ of *g*-BAs could be further lowered if 4-phonons scattering is included. The *in-plane* longitudinal acoustic (LA), transverse acoustic (TA) and *out-of-plane* flexural acoustic (FA) phonon branches contribute 28.5%, 43.1% and 26.9%, respectively. The κ of *g*-BAs are 89.3 and 137.7 W/mK before and after iteration, respectively. The large difference in the RTA and iteration

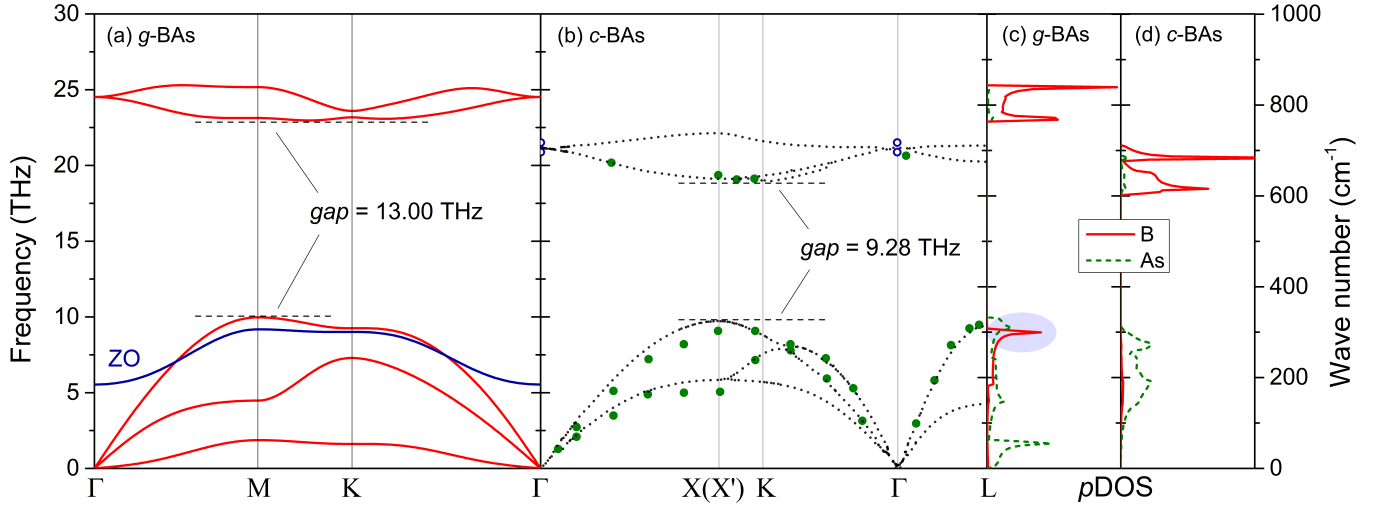


FIG. 3. The comparison of phonon dispersion of boron arsenide in 2D (*g*-BAs) with 3D (*c*-BAs). (a) The phonon dispersion of *g*-BAs along the high-symmetry points, where the *out-of-plane* flexural acoustic (FA) phonon branch shows a good quadratic behavior (Supplemental Figure 1). There exists a huge gap of 13.00 THz between the optical and acoustic phonon branches. The *z*-direction optical (ZO) phonon branch, which is below the gap, is highlighted in blue. (b) The phonon dispersion of *c*-BAs along the high-symmetry points, where dot lines in black are from theoretical calculations⁵ and blue/green points are from experimental measurements^{6,14}. The gap between the optical and acoustic phonon branches is 9.28 THz. (c,d) The partial density of states (pDOS) of (c) *g*-BAs and (d) *c*-BAs, where the contribution from boron (B) atoms to ZO is highlighted with a colored ellipse.

result means that the proportion of N-process could be large and there exists strong phonon hydrodynamics in *g*-BAs.

The lower κ of *g*-BAs than graphene is very intriguing considering the similarity of their planar honeycomb geometry structures [Fig. 2(a,b)]. In particular, the κ of *c*-BAs is comparable to diamond [Fig. 2(c)]⁵, both of which

share the same cubic structures and are the 3D counterparts of *g*-BAs and graphene, respectively [Fig. 2(a,b)]. However, when transforming from 3D to 2D, huge difference emerges that the κ of *g*-BAs (the 2D counterpart of *c*-BAs) is much lower than that of graphene (the 2D counterpart of diamond), despite the comparable κ of *c*-BAs and diamond [Fig. 2(c)]. In the following, we perform detailed analysis to achieve fundamental understanding on the anomalously lowered κ of *g*-BAs compared to *c*-BAs, diamond, and graphene. With the uncovered underlying mechanism, the generally lower κ of systems in 2D than 3D form as shown in Fig. 1 can also be well understood.

B. Large scattering phase space

Fig. 3(a) shows the phonon dispersion of *g*-BAs, in comparison with *c*-BAs [Fig. 3(b)]. It was claimed in previous study⁵ that the ultra-high κ of *c*-BAs comparable to diamond is resulted from the large phonon band gap between acoustic and optical phonon branches together with the bunching of the acoustic phonon branches. The features of the phonon dispersion of *c*-BAs analyzed based on first-principles calculations are then confirmed by experimental measurements based on inelastic *x*-ray scattering⁶, as reproduced in Fig. 3(b). When transforming from 3D *c*-BAs to 2D *g*-BAs, the phonon dispersions show some different features, which could have remarkable effect on the κ . (i) The phonon band gap in *g*-BAs is 13.00 THz, which is larger than that in *c*-BAs (9.28 THz). The larger phonon band gap is expected to not have a

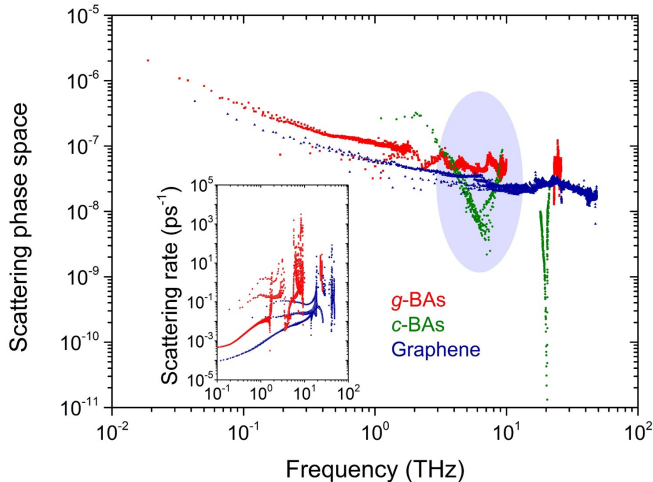


FIG. 4. Comparison of the phonon-phonon scattering phase space of *g*-BAs with *c*-BAs and graphene. The colored ellipse highlights the larger scattering phase space of *g*-BAs than *c*-BAs in the frequency range of 5-10 THz, where the ZO phonon branch lies. (Inset) The comparison of scattering rate between *g*-BAs and graphene.

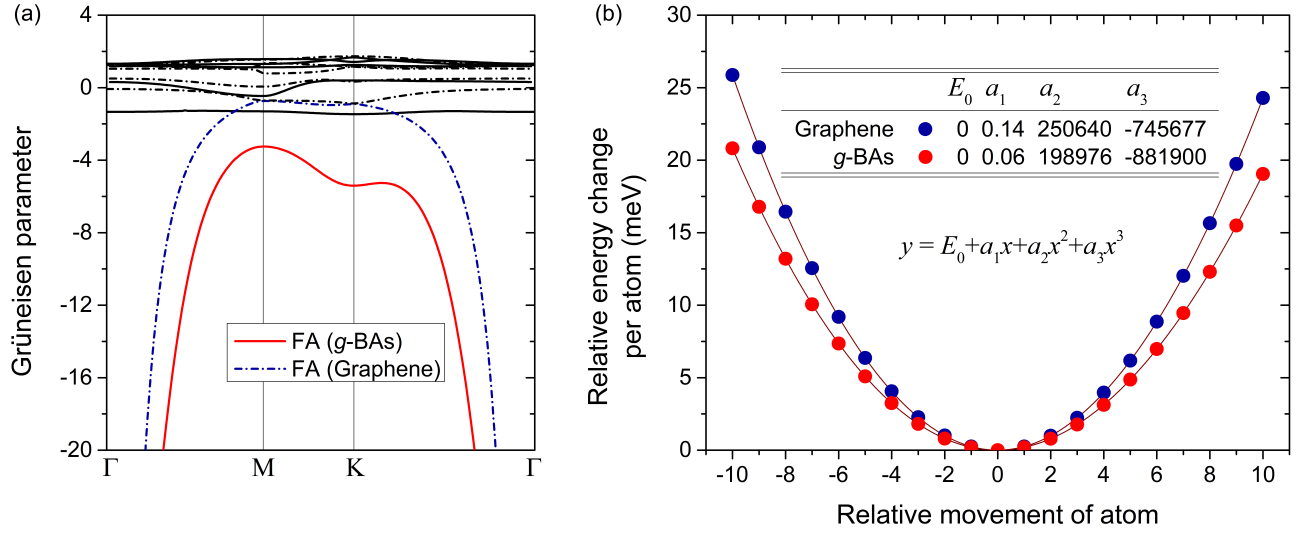


FIG. 5. Strong phonon anharmonicity in *g*-BAs. (a) Comparison of Grüneisen parameters between *g*-BAs and graphene. The colored lines highlight the Grüneisen parameters of FA phonon branch. (b) Comparison of potential energy wells between *g*-BAs and graphene. The atom is moved along the bonding direction. Points are from first-principles calculations and lines are fittings to the formula shown on site. Inset table: The fitted parameters for *g*-BAs and graphene, respectively.

negative effect on the κ for the 3-phonons scattering processes considered here. (ii) The *z*-direction optical (ZO) phonon branch in *g*-BAs is below the bandgap as highlighted in Fig. 3(a), which could lead to more scattering probability by coupling with acoustic phonon branches (especially LA). See Supplemental Note 1 and Supplemental Figure 2 for more information on the coupling as revealed by phonon-phonon scattering channels. Such coupling is absent in the 3D *c*-BAs. (iii) The bunching of acoustic phonon branches in *g*-BAs becomes weak due to the separation of the three phonon branches. The weakened bunching effect for acoustic phonon branches together with the coupling with ZO phonon branch could lead to more phonon-phonon scattering, and thus is probably responsible for the anomalously lower κ of *g*-BAs than *c*-BAs.

The ZO phonon branch in *g*-BAs is mainly contributed from the boron (B) atoms, as revealed by the partial density of states (*p*DOS) in Fig. 3(c). In fact, due to the mass difference, the optical phonon branches in both *c*-BAs and *g*-BAs are contributed from the B atoms [Fig. 3(c,d)]. With the geometry structures transformed from 3D (*c*-BAs) to 2D (*g*-BAs), the *z*-direction vibration of B atoms is totally different due to the 2D nature of bondings and structural symmetry, which lowers the frequency of ZO and provides more scattering probability in *g*-BAs by strongly coupling with acoustic phonon branches [Fig. 3(a)] (Supplemental Note 1 and Supplemental Figure 2). Such phenomena is also observed in monolayer GaN^{15,16}.

All the possible phonon-phonon scattering events quantified by the scattering phase space are determined based on the phonon dispersions by conserving both energy and crystal momentum with symmetry

included^{17–20}

$$\begin{aligned}\omega_j(\vec{q}) \pm \omega_{j'}(\vec{q}') &= \omega_{j''}(\vec{q}'') , \\ \vec{q} \pm \vec{q}' &= \vec{q}'' + \vec{K} ,\end{aligned}\quad (2)$$

where ω is the frequency of phonon modes ($\hbar\omega$ is the corresponding energy), \vec{q} is the wave vector. Normal process corresponds to $\vec{K} = 0$, while Umklapp process corresponds to $\vec{K} \neq 0$. Fig. 4 presents the phase space of 3-phonons scattering in *g*-BAs, in comparison with that in *c*-BAs. The scattering phase space in *c*-BAs is small due to the large acoustic-optical phonon band gap, which is responsible for the ultra-high κ of *c*-BAs as analyzed in previous study⁵. However, the scattering phase space in *g*-BAs is larger than that in *c*-BAs, especially for the frequency range of 5–10 THz (Fig. 4), despite the larger gap in *g*-BAs than *c*-BAs [Fig. 3(a,b)]. The enhanced scattering probability could be attributed to the weakened bunching effect for acoustic phonon branches together with their coupling with ZO phonon branch in *g*-BAs [Fig. 3(a)], which partially explains the anomalously lower κ of *g*-BAs than *c*-BAs.

We also compare the phase spaces between *g*-BAs and graphene. It is found that the overall scattering phase space in *g*-BAs is larger than that in graphene. Thus, the anomalously lower κ of *g*-BAs than graphene is understandable despite their similar structures. However, it should be noted that the difference in the scattering phase space is much less than one order of magnitude, which cannot fully explain the large difference in the scattering rate (Inset of Fig. 4) and further the more than one order of magnitude lower κ of *g*-BAs (137.70 W/mK) than graphene (3094.98 W/mK). Therefore, there should be some other mechanism also responsible for the anomalously low κ of *g*-BAs beyond the scattering phase space.

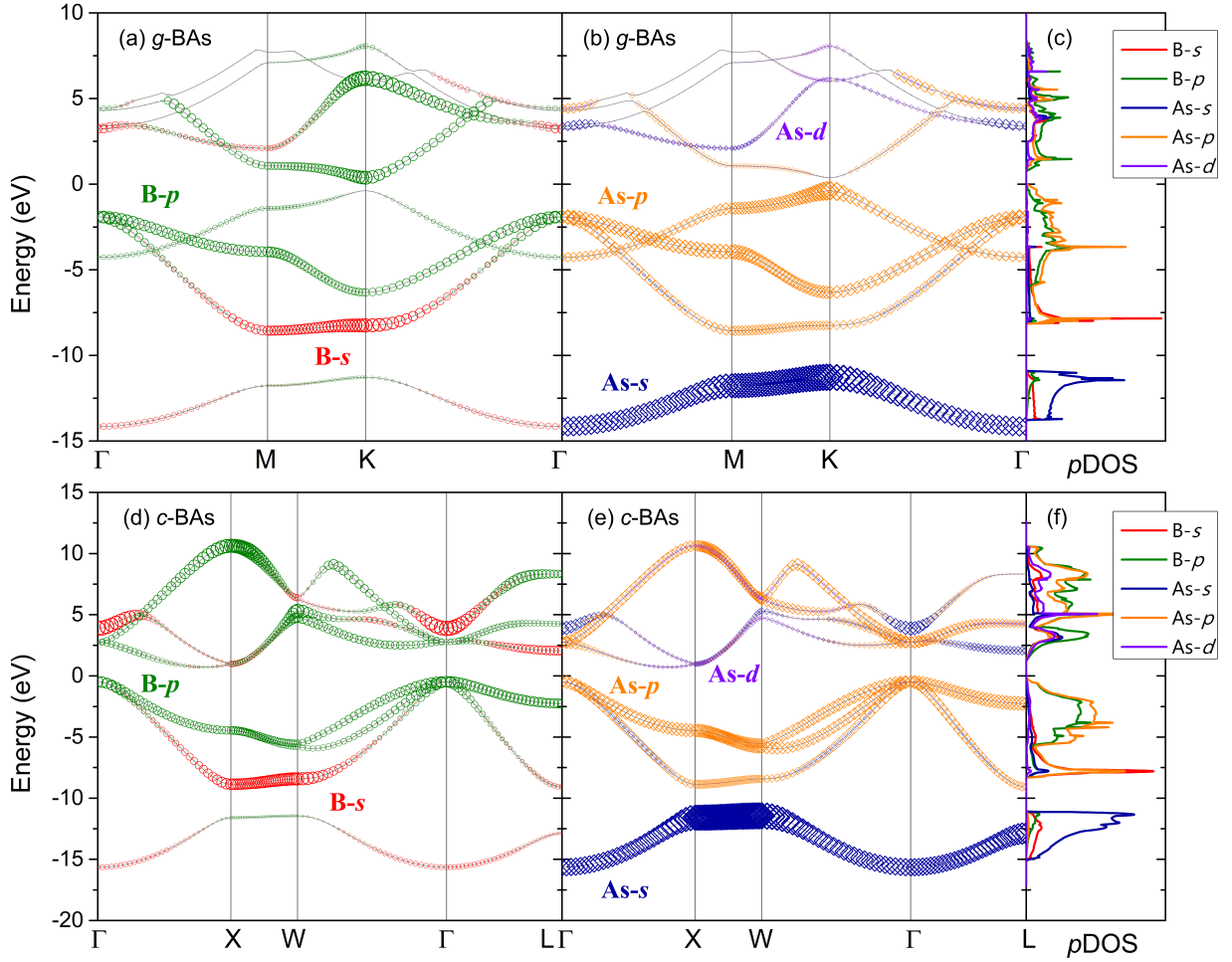


FIG. 6. Orbitals projected electronic structures, revealing the non-bonding lone-pair As-s electrons. (a,b,c) The orbitals projected (a,b) electronic band structures and (c) density of states (DOS) for *g*-BAs. The electronic structures are projected to (a) B-s/*p* and (b) As-s/*p/d* orbitals. (d,e,f) Similar figures for *c*-BAs in comparison.

C. Strong phonon anharmonicity

It is well known that the phonon lifetime is governed by two factors: phonon-phonon scattering phase space and strength. The phonon-phonon scattering strength describes how strong is the phonon-phonon scattering process, which is governed by the anharmonic nature of the system. The Grüneisen parameter that describes the phonon anharmonicity can be calculated based on the change of phonon frequency with respect to the volume change

$$\gamma = -\frac{V}{\omega} \frac{\partial \omega}{\partial V}. \quad (3)$$

Fig. 5(a) shows the obtained Grüneisen parameter of *g*-BAs, in comparison with graphene. The FA phonon branch possess the largest magnitude of Grüneisen parameter for both *g*-BAs and graphene, and the magnitude is larger in *g*-BAs than in graphene, revealing the stronger phonon anharmonicity in *g*-BAs. Thus, the more than one order of magnitude lower κ of *g*-BAs than

graphene can be well understood by combining the larger scattering phase space (Fig. 4) and the stronger phonon anharmonicity in *g*-BAs.

The phonon anharmonicity can also be intuitively revealed by the potential energy well. To have an explicit look at the anharmonicity, the potential energy wells (potential energy changes per atom due to the atomic displacement) of *g*-BAs and graphene are plotted in Fig. 5(b) for comparison. Both the potential wells are asymmetric with respect to the positive and negative atomic displacements, indicating the asymmetry in the ability of an atom vibrating around its equilibrium position and the nonlinear dependence of restoring forces on atomic displacement amplitudes, which is the direct evidence of the anharmonicity^{21–23}. We further fit the calculated points for *g*-BAs and graphene, respectively, with the polynomial

$$y = E_0 + a_1x + a_2x^2 + a_3x^3, \quad (4)$$

where y is the relative energy change per atom, and x is the relative movement of atom. The fitted param-

ters for *g*-BAs and graphene are listed in the table as inset in Fig. 5(b). The fitted quadric (a_2) and cubic (a_3) terms correspond to the harmonicity and anharmonicity, respectively. The relatively smaller harmonic term in *g*-BAs reveals the weaker bonding strength of B-As bond than C-C band in graphene, and the relatively larger magnitude of the anharmonic term reveals stronger phonon anharmonicity in *g*-BAs.

D. Lone-pair electrons

To gain deep insight into the origin of the strong phonon anharmonicity in *g*-BAs, we further perform fundamental analysis on the electronic structures to uncover the underlying mechanism. We will show that the strong phonon anharmonicity in *g*-BAs is fundamentally driven by the stereochemically active lone-pair electrons due to the special orbital hybridization.

The orbital projected electronic structures [band structure and density of states (DOS)] of *g*-BAs are depicted in Fig. 6(a,b,c). Direct band gap (~ 0.75 eV) emerges in *g*-BAs, which is different from the indirect band gap in *c*-BAs [Fig. 6(d,e)]. As shown in Fig. 6(a,b,c), the bonding states in *g*-BAs are governed by the B-*s/p* and As-*p* orbitals. As for B atom, all the 3 valence electrons are involved in the formation of B-As σ bonds due to the sp^2 -hybridization [Fig. 6(a)]. The situation is totally different for As atom which possesses 5 valence electrons. The As-*s* orbital is largely (~ 10 eV) confined below the valence band, forming an isolated band [Fig. 6(b)]. Consequently, only the As-*p* orbitals contribute to the B-As σ bonds. Thus, the s^2 electrons in the s^2p^3 valence configuration of As atom do not participate in the bonding and thus form lone-pair around the As atoms. To have an intuitive view on the lone-pair As-*s* electrons, we plot the electron localization function (ELF) in Fig. 7. The ELF displays the location and size of bonding and lone-pair electron, which is powerful in interpreting chemical bonding patterns²¹. The ELF values range from 0 to 1, where 0 means no electron, 0.5 corresponds to the electron-gas-like pair probability, and 1 corresponds to perfect localization. It is well known that in graphene the C-C σ bonds are contributed from the hybridized C- $s/p_x/p_y$ orbitals and the solo C- p_z orbital forms the π bonds and the electronic Dirac cone (Supplemental Figure 3)²⁴. Thus, there is no lone-pair electrons formed in graphene. By comparing the side views of the ELF between *g*-BAs [Fig. 7(b)] and graphene [Fig. 7(a)], it can be clearly seen that there are electrons localized around As atom that are not bonded, which are the lone-pair electrons.

It was proposed that lone-pair electrons could lead to low κ ²⁵. The principle underlying the concept is that the overlapping wave functions of lone-pair electrons with valence (bonding) electrons from adjacent atoms would induce nonlinear electrostatic forces upon thermal agitation, leading to increased phonon anharmonicity in the

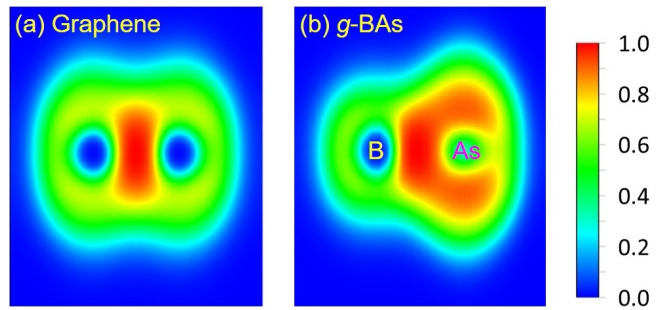


FIG. 7. Side views of the electron localization function (ELF) for (a) graphene and (b) *g*-BAs. The comparison reveals the stereochemically activated lone-pair electrons in *g*-BAs, which are non-bonding around arsenide (As) atom.

lattice and thus reducing the κ ^{25–31}. Due to the orbital distribution in the same energy range and wave functions overlap as shown in Figs. 6(a,b,c) and 7(b), the non-bonding lone-pair As-*s* electrons interact with the covalently bonding electrons of adjacent B atoms in *g*-BAs. The interactions induce nonlinear electrostatic force among atoms when they thermally vibrate around the equilibrium positions³². The nonlinear electrostatic force originates from the asymmetric change of the hybridization between As-*s* and B-*s/p* for the atomic motion, as revealed by the *p*DOS evolution in Supplemental Figure 4. A more asymmetric potential energy well is induced together with the additional nonlinear electrostatic force [Fig. 5(b)], which leads to the strong phonon anharmonicity in *g*-BAs [Fig. 5(a)] and significantly reduces the κ of *g*-BAs [Fig. 2(c)].

The form of orbital hybridizations in *c*-BAs are highly consistent with those in *g*-BAs as shown in Fig. 6, which means that lone-pair As-*s* electrons also emerge around As atoms in *c*-BAs. However, no strong phonon anharmonicity is induced in *c*-BAs by the lone-pair As-*s* electrons despite the similar orbital hybridization form as *g*-BAs, which is due to the different bonding nature and coordination environment between 3D and 2D geometry structures. Due to the perfect octahedral coordination of As atoms in *c*-BAs resulted from its cubic structure [Fig. 2(b)], four equivalent valence bonds are formed. Thus, the lone-pair electrons in *c*-BAs are stereochemically inactive, which has no effect on the phonon anharmonicity. In contrast, for *g*-BAs possessing planar structure, no pyramidal geometry is formed for the B-As bonds. Consequently, lone-pair As-*s* electrons are located at both sides of the 2D structure plane in *g*-BAs [Fig. 7(b)], which is different from that in 3D bulk systems of *c*-BAs. Thus, strong phonon anharmonicity exist in *g*-BAs due to the stereochemical activity of the lone-pair As-*s* electrons in the geometric form of planar structure.

E. Extention to other systems

It was shown above that bond nanodesigning by changing the coordination environment is an effective approach for realizing low κ , which would benefit the design of thermoelectric devices with improved performance. The approaches can also be applied to other materials beyond the BAs systems studied here, for instance, the class of group III-V compounds (*e.g.* BN, AlN, GaN, *etc.*), where lone-pair electrons also exist (Fig. 1). Strong phonon anharmonicity and low κ could be achieved with the stereochemically activated lone-pair electrons, which can be realized by breaking the perfect octahedral coordination [Fig. 2(a,b)]. Note that the 2D structures of the systems presented in Fig. 1 are all planar except silicene. For the systems with buckled structures in 2D form, such as silicon *vs.* silicene, the situation will be different due to the broken symmetry-based selection rule for phonon-phonon scattering^{15,16,33}. It is found that there exists a strong correlation between the electronegativity difference and the κ modulation for binary compounds (Fig. 1). The effect of κ modulation by stereochemically activating the lone-pair electrons is weaker with a larger electronegativity difference. The reason may lie in the contribution to phonon anharmonicity of the electronegativity difference¹⁵. Other approaches could also have the same effects on the κ modulation that make the lone-pair electrons stereochemically active, such as nanostructuring. Alternatively, it would be also possible by substituting the atoms in ordinary materials with special atoms that can form non-bonding lone-pair electrons, such as nitrogen, phosphorus, arsenic, *etc.*

Note that the κ of the studied systems here does not achieve an ultralow value, which may limit their direct applications in thermoelectrics. However, if the approach of activating lone-pair electrons is combined with the commonly used strategy of nanostructuring, ultralow κ desirable for thermoelectrics could be effectively achieved. For example, experimental measurements have already demonstrated that the κ of BAs can be suppressed by the arsenic deficiency or vacancy in the BAs sample¹¹ and the phonon-boundary scattering in BAs microstructures^{12,13}. However, the obtained κ of BAs is still too high, which limits its potential applications in thermoelectrics, despite its quite large Seebeck coefficient and thermoelectric power factor¹³. If the lone-pair electrons in the BAs system can be stereochemically activated, the κ could be further reduced, which would improve the thermoelectric performance in the experimental setup. Besides, due to the intrinsic high κ , BAs also shows promising applications in efficient heat dissipation of electronics. When incorporating it into conventional semiconducting devices for heat dissipation, special attention should be paid to avoid activating the lone-pair electrons in BAs based nanostructures for keeping the high κ .

III. CONCLUSIONS

In summary, by cutting the 3D cubic structure of *c*-BAs at the (111) cross section, more than one order of magnitude lowered κ is achieved in the resultant 2D system of *g*-BAs with similar structure as graphene, which shows that bond nanodesigning by transforming the materials into nanoscale with the broken coordination environment could be an effective approach for realizing low κ . Based on the systematic study on the thermal transport properties of *g*-BAs comparing with *c*-BAs, diamond, and graphene (*c*-BAs \rightarrow *g*-BAs *vs.* diamond \rightarrow graphene), the underlying mechanism for the substantially lowered κ in the case of '*c*-BAs \rightarrow *g*-BAs' lies in two aspects: 1) Resulted from mass difference and 2D nature of bondings and structural symmetry, the weakened bunching effect for acoustic phonon branches together with their coupling with ZO phonon branch play a key role in driving large probability of phonon-phonon scattering. 2) Strong phonon anharmonicity is fundamentally driven by the stereochemically activated lone-pair electrons in *g*-BAs. Due to the special orbital hybridization, the s^2 electrons in the s^2p^3 valence configuration of As atom do not participate in the bonding but form lone-pair instead. When transforming from the 3D cubic structure of *c*-BAs to 2D planar structure of *g*-BAs, the lone-pair As-*s* electrons become stereochemically activated due to the break of the perfect octahedral coordination of As atoms in *c*-BAs, which leads to strong phonon anharmonicity in *g*-BAs. Similar concept can be also extended to other systems with lone-pair electrons beyond BAs, such as group III-V compounds (*e.g.* BN, AlN, GaN, *etc.*), where a strong correlation between κ modulation and electronegativity difference for binary compounds is found. Thus, the lone-pair electrons combined with a small electronegativity difference could be the indicator of lowering κ through bond nanodesigning to change the coordination environment. The proposed approach for realizing low κ and the underlying mechanism uncovered in this study would shed light on future research involving novel materials for energy applications.

IV. COMPUTATIONAL DETAILS

All the first-principles calculations are performed based on the density functional theory (DFT) as implemented in the Vienna *ab initio* simulation package (VASP)³⁵. The Perdew-Burke-Ernzerhof (PBE)³⁶ of generalized gradient approximation (GGA) is chosen as the exchange-correlation functional for describing boron arsenide (BAs) systems, which is produced using the projector augmented wave (PAW) method³⁷. Based on careful convergence test, the kinetic energy cutoff of wave function is set as 800 eV for all the DFT calculations. For the 2D systems, a large vacuum spacing is necessary to hinder the interactions arising from the employed periodic boundary conditions, which is set as 20 Å along the

out-of-plane direction. The Monkhorst-Pack³⁸ k -meshes of $15 \times 15 \times 1$ and $2 \times 2 \times 1$ are used to sample the Brillouin zone (BZ) for the structure optimizations and supercell force calculations, respectively, with the energy convergence threshold set as 10^{-8} eV. The structure optimization is fully conducted with no limitation until the maximal Hellmann-Feynman force acting on each atom is less than 10^{-9} eV/Å.

For the supercell force calculations to obtain interatomic force constants (IFCs), a $5 \times 5 \times 1$ supercell is constructed based on the convergence of the phonon dispersion with respect to the supercell size. The cutoff radius (r^{cutoff}) introduced during the calculations of the anharmonic IFCs is also fully tested, which is used to discard the interactions between atoms with distance larger than a certain value for practical purposes. The r^{cutoff} of 10th nearest neighbors (~ 0.94 nm) is found to be large enough to obtain converged and reliable κ ³⁹. The space group symmetry properties are used to reduce the computational cost and the translational and rotational invariance of IFCs are enforced using the Lagrange multiplier method^{40–42}. With the anharmonic IFCs, the scattering matrix can be constructed, based on which one can calculate all the three-phonon scattering rates and then obtain phonon lifetime. The Born effective charge (Z^*) and dielectric constant (ϵ) obtained based on the density functional perturbation theory (DFPT) are included for taking into account of long-range electrostatic interactions. The thickness for calculating κ is chosen as the van der Waals diameter (3.7 Å). The κ is obtained by solving the linearized phonon BTE using an iterative procedure as implemented in the ShengBTE package based on the IFCs^{42,43}. More information can be found in Supplemental Note 2.

V. ACKNOWLEDGMENTS

Simulations were performed with computing resources granted by RWTH Aachen University under projects rwth0366. M.H. acknowledges the start-up fund from the University of South Carolina. Z.Q. is supported by the National Natural Science Foundation of China (Grant No. 11847158) and the China Postdoctoral Science Foundation (2018M642776).

VI. SUPPLEMENTAL INFORMATION

Supplemental Table for the specific κ of the typical systems in 3D and 2D forms;

Supplemental Figures for 1) the phonon dispersion showing quadratic behavior of FA, 2) phonon-phonon scattering channels of FA, 3) orbitals projected electronic structures for graphene, 4) p DOS evolution for g -BAs due to atomic motion, and 5) normalized κ for several typical 2D materials;

Supplemental Notes for 1) phonon-phonon scatter-

ing channels and 2) more information on computational methods.

VII. DATA AVAILABILITY

The data that support the findings of this study are available from the corresponding author upon reasonable request.

- ¹K. Biswas, J. He, I. D. Blum, C.-I. Wu, T. P. Hogan, D. N. Seidman, V. P. Dravid, M. G. Kanatzidis, High-performance bulk thermoelectrics with all-scale hierarchical architectures, *Nature* 489 (2012) 414. doi:10.1038/nature11439.
URL <http://dx.doi.org/10.1038/nature11439>
- ²G. Qin, Q.-B. Yan, Z. Qin, S.-Y. Yue, H.-J. Cui, Q.-R. Zheng, G. Su, Hinge-like structure induced unusual properties of black phosphorus and new strategies to improve the thermoelectric performance, *Sci. Rep.* 4 (6946) (2014) 6946.
- ³L.-D. Zhao, G. Tan, S. Hao, J. He, Y. Pei, H. Chi, H. Wang, S. Gong, H. Xu, V. P. Dravid, Ultrahigh power factor and thermoelectric performance in hole-doped single-crystal SnSe , *Science* 351 (2016) 141–144.
- ⁴X. Zhang, H. Xie, M. Hu, H. Bao, S. Yue, G. Qin, G. Su, Thermal conductivity of silicene calculated using an optimized stillinger-weber potential, *Phys. Rev. B* 89 (2014) 054310. doi:10.1103/PhysRevB.89.054310.
URL <http://link.aps.org/doi/10.1103/PhysRevB.89.054310>
- ⁵L. Lindsay, D. A. Broido, T. L. Reinecke, First-principles determination of ultrahigh thermal conductivity of boron arsenide: A competitor for diamond?, *Phys. Rev. Lett.* 111 (2013) 025901. doi:10.1103/PhysRevLett.111.025901.
URL <http://link.aps.org/doi/10.1103/PhysRevLett.111.025901>
- ⁶H. Ma, C. Li, S. Tang, J. Yan, A. Alatas, L. Lindsay, B. C. Sales, Z. Tian, Boron arsenide phonon dispersion from inelastic x-ray scattering: Potential for ultrahigh thermal conductivity, *Phys. Rev. B* 94 (2016) 220303. doi:10.1103/PhysRevB.94.220303.
URL <https://link.aps.org/doi/10.1103/PhysRevB.94.220303>
- ⁷T. Feng, L. Lindsay, X. Ruan, Four-phonon scattering significantly reduces intrinsic thermal conductivity of solids, *Phys. Rev. B* 96 (2017) 161201. doi:10.1103/PhysRevB.96.161201.
URL <https://link.aps.org/doi/10.1103/PhysRevB.96.161201>
- ⁸J. S. Kang, M. Li, H. Wu, H. Nguyen, Y. Hu, Experimental observation of high thermal conductivity in boron arsenide, *Science* <http://science.sciencemag.org/content/early/2018/07/03/science.aat5522.full.pdf>, doi:10.1126/science.aat5522.
URL <http://science.sciencemag.org/content/early/2018/07/03/science.aat5522>
- ⁹S. Li, Q. Zheng, Y. Lv, X. Liu, X. Wang, P. Y. Huang, D. G. Cahill, B. Lv, High thermal conductivity in cubic boron arsenide crystals, *Science* <http://science.sciencemag.org/content/early/2018/07/03/science.aat8982.full.pdf>, doi:10.1126/science.aat8982.
URL <http://science.sciencemag.org/content/early/2018/07/03/science.aat8982>
- ¹⁰F. Tian, B. Song, X. Chen, N. K. Ravichandran, Y. Lv, K. Chen, S. Sullivan, J. Kim, Y. Zhou, T.-H. Liu, M. Goni, Z. Ding, J. Sun, G. A. G. U. Gamage, H. Sun, H. Ziyadee, S. Huyan, L. Deng, J. Zhou, A. J. Schmidt, S. Chen, C.-W. Chu, P. Y. Huang, D. Broido, L. Shi, G. Chen, Z. Ren, Unusual high thermal conductivity in boron arsenide bulk crystals, *Science* <http://science.sciencemag.org/content/early/2018/07/03/science.aat7932.full.pdf>, doi:10.1126/science.aat7932.
URL <http://science.sciencemag.org/content/early/2018/07/03/science.aat7932>

- ¹¹B. Lv, Y. Lan, X. Wang, Q. Zhang, Y. Hu, A. J. Jacobson, D. Broido, G. Chen, Z. Ren, C.-W. Chu, Experimental study of the proposed super-thermal-conductor: Bas, Appl. Phys. Lett. 106 (2015) 074105. doi:10.1063/1.4913441. URL <https://doi.org/10.1063/1.4913441>
- ¹²D. A. Broido, L. Lindsay, T. L. Reinecke, *Ab initio* study of the unusual thermal transport properties of boron arsenide and related materials, Phys. Rev. B 88 (2013) 214303. doi:10.1103/PhysRevB.88.214303. URL <http://link.aps.org/doi/10.1103/PhysRevB.88.214303>
- ¹³J. Kim, D. A. Evans, D. P. Sellan, O. M. Williams, E. Ou, A. H. Cowley, L. Shi, Thermal and thermoelectric transport measurements of an individual boron arsenide microstructure, Appl. Phys. Lett. 108 (2016) 201905. doi:10.1063/1.4950970. URL <https://doi.org/10.1063/1.4950970>
- ¹⁴R. G. Greene, H. Luo, A. L. Ruoff, S. S. Trail, F. J. DiSalvo, Pressure induced metastable amorphization of bas: Evidence for a kinetically frustrated phase transformation, Phys. Rev. Lett. 73 (1994) 2476–2479. doi:10.1103/PhysRevLett.73.2476. URL <https://link.aps.org/doi/10.1103/PhysRevLett.73.2476>
- ¹⁵Z. Qin, G. Qin, X. Zuo, Z. Xiong, M. Hu, Orbital driven low thermal conductivity of monolayer gallium nitride (gan) with planar honeycomb structure: a comparative study, Nanoscale 9 (2017) 4295–4309. doi:10.1039/C7NR01271C. URL <http://dx.doi.org/10.1039/C7NR01271C>
- ¹⁶G. Qin, Z. Qin, H. Wang, M. Hu, Anomalously temperature-dependent thermal conductivity of monolayer gan with large deviations from the traditional $1/t$ law, Phys. Rev. B 95 (2017) 195416. doi:10.1103/PhysRevB.95.195416. URL <https://link.aps.org/doi/10.1103/PhysRevB.95.195416>
- ¹⁷A. Ward, D. A. Broido, Intrinsic phonon relaxation times from first-principles studies of the thermal conductivities of Si and Ge, Phys. Rev. B 81 (2010) 085205. doi:10.1103/PhysRevB.81.085205. URL <http://link.aps.org/doi/10.1103/PhysRevB.81.085205>
- ¹⁸A. Ward, D. A. Broido, D. A. Stewart, G. Deinzer, *Ab initio* theory of the lattice thermal conductivity in diamond, Phys. Rev. B 80 (2009) 125203. doi:10.1103/PhysRevB.80.125203. URL <http://link.aps.org/doi/10.1103/PhysRevB.80.125203>
- ¹⁹M. Omini, A. Sparavigna, Beyond the isotropic-model approximation in the theory of thermal conductivity, Phys. Rev. B 53 (1996) 9064–9073. doi:10.1103/PhysRevB.53.9064. URL <http://link.aps.org/doi/10.1103/PhysRevB.53.9064>
- ²⁰L. Lindsay, D. A. Broido, Three-phonon phase space and lattice thermal conductivity in semiconductors, J. Phys.: Condens. Matter 20 (16) (2008) 165209. URL <http://stacks.iop.org/0953-8984/20/i=16/a=165209>
- ²¹G. Qin, X. Zhang, S.-Y. Yue, Z. Qin, H. Wang, Y. Han, M. Hu, Resonant bonding driven giant phonon anharmonicity and low thermal conductivity of phosphorene, Phys. Rev. B 94 (2016) 165445. doi:10.1103/PhysRevB.94.165445. URL <http://link.aps.org/doi/10.1103/PhysRevB.94.165445>
- ²²W. G. Zeier, A. Zevakink, Z. M. Gibbs, G. Hautier, M. G. Kanatzidis, G. J. Snyder, Thinking like a chemist: Intuition in thermoelectric materials, Angew. Chem. Int. Ed. 55 (2016) 2–18. doi:10.1002/anie.201508381. URL <http://dx.doi.org/10.1002/anie.201508381>
- ²³L.-D. Zhao, C. Chang, G. Tan, M. G. Kanatzidis, Snse: a remarkable new thermoelectric material, Energy Environ. Sci. 9 (2016) 3044–3060. doi:10.1039/C6EE01755J. URL <http://dx.doi.org/10.1039/C6EE01755J>
- ²⁴A. A. Balandin, D. L. Nika, Phononics in low-dimensional materials, Materials Today 15 (6) (2012) 266 – 275. doi:10.1016/S1369-7021(12)70117-7. URL <http://www.sciencedirect.com/science/article/pii/S1369702112701177>
- ²⁵A. V. Petrov, E. L. Shtrum, Sov. Phys. Solid State 4 (1962) 1061.
- ²⁶D. T. Morelli, V. Jovovic, J. P. Heremans, Intrinsically minimal thermal conductivity in cubic $\text{Im}\bar{4}2\text{m}$ semiconductors, Phys. Rev. Lett. 101 (2008) 035901. doi:10.1103/PhysRevLett.101.035901. URL <http://link.aps.org/doi/10.1103/PhysRevLett.101.035901>
- ²⁷E. J. Skoug, D. T. Morelli, Role of lone-pair electrons in producing minimum thermal conductivity in nitrogen-group chalcogenide compounds, Phys. Rev. Lett. 107 (2011) 235901. doi:10.1103/PhysRevLett.107.235901. URL <http://link.aps.org/doi/10.1103/PhysRevLett.107.235901>
- ²⁸M. D. Nielsen, V. Ozolins, J. P. Heremans, Lone pair electrons minimize lattice thermal conductivity, Energy Environ. Sci. 6 (2013) 570–578. doi:10.1039/C2EE23391F. URL <http://dx.doi.org/10.1039/C2EE23391F>
- ²⁹J. P. Heremans, Thermoelectric materials: The anharmonicity blacksmith, Nat. Phys. 11 (2015) 990–991. doi:10.1038/nphys3542. URL <http://dx.doi.org/10.1038/nphys3542>
- ³⁰M. K. Jana, K. Pal, U. V. Waghmare, K. Biswas, The origin of ultralow thermal conductivity in inte: Lone-pair-induced anharmonic rattling, Angew. Chem. Int. Ed. 55 (2016) 7792–7796. doi:10.1002/anie.201511737. URL <http://dx.doi.org/10.1002/anie.201511737>
- ³¹Y. Xiao, C. Chang, Y. Pei, D. Wu, K. Peng, X. Zhou, S. Gong, J. He, Y. Zhang, Z. Zeng, L.-D. Zhao, Origin of low thermal conductivity in snse, Phys. Rev. B 94 (2016) 125203. doi:10.1103/PhysRevB.94.125203. URL <http://link.aps.org/doi/10.1103/PhysRevB.94.125203>
- ³²G. Qin, Z. Qin, H. Wang, M. Hu, Lone-pair electrons induced anomalous enhancement of thermal transport in strained planar two-dimensional materials, Nano Energy 50 (2018) 425–430. URL <http://www.sciencedirect.com/science/article/pii/S2211285518303574>
- ³³L. Lindsay, D. A. Broido, N. Mingo, Flexural phonons and thermal transport in graphene, Phys. Rev. B 82 (2010) 115427. doi:10.1103/PhysRevB.82.115427. URL <http://link.aps.org/doi/10.1103/PhysRevB.82.115427>
- ³⁴B. Peng, H. Zhang, H. Shao, Y. Xu, G. Ni, R. Zhang, H. Zhu, Phonon transport properties of two-dimensional group-iv materials from *ab initio* calculations, Phys. Rev. B 94 (2016) 245420. doi:10.1103/PhysRevB.94.245420. URL <https://link.aps.org/doi/10.1103/PhysRevB.94.245420>
- ³⁵G. Kresse, J. Furthmüller, Efficient iterative schemes for *ab initio* total-energy calculations using a plane-wave basis set, Phys. Rev. B 54 (1996) 11169–11186. doi:10.1103/PhysRevB.54.11169. URL <http://link.aps.org/doi/10.1103/PhysRevB.54.11169>
- ³⁶J. P. Perdew, K. Burke, M. Ernzerhof, Generalized gradient approximation made simple, Phys. Rev. Lett. 77 (1996) 3865–3868. doi:10.1103/PhysRevLett.77.3865. URL <http://link.aps.org/doi/10.1103/PhysRevLett.77.3865>
- ³⁷G. Kresse, D. Joubert, From ultrasoft pseudopotentials to the projector augmented-wave method, Phys. Rev. B 59 (1999) 1758–1775. doi:10.1103/PhysRevB.59.1758. URL <http://link.aps.org/doi/10.1103/PhysRevB.59.1758>
- ³⁸H. J. Monkhorst, J. D. Pack, Special points for brillouin-zone integrations, Phys. Rev. B 13 (1976) 5188–5192. doi:10.1103/PhysRevB.13.5188. URL <http://link.aps.org/doi/10.1103/PhysRevB.13.5188>
- ³⁹G. Qin, M. Hu, Accelerating evaluation of converged lattice thermal conductivity, npj Computational Materials 4 (2018) 3. doi:Qin2018. URL <https://doi.org/10.1038/s41524-017-0058-3>
- ⁴⁰A. Togo, F. Oba, I. Tanaka, First-principles calculations of the ferroelastic transition between rutile-type and CaCl_2 -type SiO_2 at high pressures, Phys. Rev. B 78 (2008) 134106.
- ⁴¹K. Esfarjani, H. T. Stokes, Method to extract anharmonic force constants from first principles calculations, Phys. Rev. B 77 (2008) 144112. doi:10.1103/PhysRevB.77.144112. URL <http://link.aps.org/doi/10.1103/PhysRevB.77.144112>

⁴²W. Li, L. Lindsay, D. A. Broido, D. A. Stewart, N. Mingo, Thermal conductivity of bulk and nanowire $\text{Mg}_2\text{Si}_x\text{Sn}_{1-x}$ alloys from first principles, Phys. Rev. B 86 (2012) 174307. doi: 10.1103/PhysRevB.86.174307.
URL <http://link.aps.org/doi/10.1103/PhysRevB.86.174307>

⁴³W. Li, J. Carrete, N. A. Katcho, N. Mingo, Shengbte: A solver of the boltzmann transport equation for phonons, Comput. Phys. Commun. 185 (6) (2014) 1747 – 1758. doi:<http://dx.doi.org/10.1016/j.cpc.2014.02.015>.
URL <http://www.sciencedirect.com/science/article/pii/S0010465514000484>